Journal of
Manufacturing and Materials Processing

MDPI

Article

Geometric and Mechanical Properties of Ti6Al4V Skeletal Gyroid Structures Produced by Laser Powder Bed Fusion for Biomedical Implants

Cong Hou [1,*], Max Goris [1], Dries Rosseel [1], Bey Vrancken [1,2] and Kathleen Denis [1,*]

[1] Department of Mechanical Engineering, KU Leuven, Celestijnenlaan 300, 3001 Leuven, Belgium; max.goris@hotmail.com (M.G.); dries.rosseel@outlook.com (D.R.); bey.vrancken@kuleuven.be (B.V.)
[2] Flanders Make@KU Leuven, 3001 Leuven, Belgium
* Correspondence: cong.hou@kuleuven.be (C.H.); kathleen.denis@kuleuven.be (K.D.)

Abstract: Skeletal gyroid structures possess promising applications in biomedical implants, owing to their smooth and continuously curved surfaces, open porosity, and customisable mechanical properties. This study simulated the geometric properties of Ti6Al4V skeletal gyroid structures, with relative densities ranging from 1.83% to 98.17%. The deformation behaviour of these structures was investigated through a combination of uniaxial compression tests and simulations, within a relative density range of 13.33% to 50% (simulation) and 15.19% to 41.69% (experimental tests). The results established explicit analytical correlations of pore size and strut diameter with the definition parameters of the structures, enabling precise control of these dimensions. Moreover, normalised Young's modulus (ranging from 1.05% to 20.77% in simulations and 1.65% to 15.53% in tests) and normalised yield stress (ranging from 1.75% to 17.39% in simulations and 2.09% to 13.95% in tests) were found to be power correlated with relative density. These correlations facilitate the design of gyroid structures with low stiffness to mitigate the stress-shielding effect. The presence of macroscopic 45° fractures in the gyroid structures confirmed that the primary failure mechanism is induced by shear loads. The observed progressive failure and plateau region proved the bending-dominant behaviour and highlighted their excellent deformability. Additionally, the anisotropy of gyroid structures was confirmed through variations in stress and strain concentrations, deformation behaviour, and Young's modulus under different loading directions.

Keywords: gyroid structure; porosity; Ti6Al4V; laser powder bed fusion; Young's modulus; anisotropy

Citation: Hou, C.; Goris, M.; Rosseel, D.; Vrancken, B.; Denis, K. Geometric and Mechanical Properties of Ti6Al4V Skeletal Gyroid Structures Produced by Laser Powder Bed Fusion for Biomedical Implants. *J. Manuf. Mater. Process.* **2024**, *8*, 256. https://doi.org/10.3390/jmmp8060256

Academic Editors: Bin Zhang, Amirpasha Moetazedian and Peter Zioupos

Received: 8 October 2024
Revised: 8 November 2024
Accepted: 11 November 2024
Published: 13 November 2024

1. Introduction

Lattice structures are widely recognised for their excellent properties. Among various lattice structures, gyroid structures, a unique type of triply periodic minimal surface (TPMS) lattice structure, are defined by implicit mathematical equations. These structures can be categorised into skeletal gyroid structures, created by filling the void between the TPMS, and sheet-based TPMS lattice structures, where a thickness is assigned to each TPMS [1]. Skeletal gyroid structures exhibit promising potential in biomedical implant applications. Adjusting the parameters in the mathematical equations [2] allows for easy tuning of relative density and mechanical properties. In contrast to conventional strut-based lattice structures, prone to stress concentration at strut junctions, the smooth and continuous TPMS surfaces facilitate seamless geometric transition and provide biomorphic advantages for cells [3]. For the remainder of this paper, skeletal gyroid structures will be referred to as gyroid structures.

The manufacturing of complex geometries like gyroid structures typically involves additive manufacturing technologies. Laser powder bed fusion (LPBF) is one of the most commonly used processes for the additive manufacturing of metal structures. However,

defects such as internal pores exist in LPBF-manufactured structures [4,5], which can negatively affect their mechanical properties. Therefore, it is essential to apply suitable process parameters and scan strategies [6], especially as these may differ for porous structures compared to bulky parts.

Healthy human bone needs sufficient stimuli to maintain its density and strength. Without sufficient stimulation, the stress-shielding effect can occur. For instance, when using stiff metal implants, most of the load is borne by the implant, rather than distributed to the surrounding bone. This could lead to bone resorption and weakening over time [7]. Applying gyroid structures in biomedical implants can help mitigate the stress shielding effect and promote osseointegration. The low stiffness of porous gyroid structures shows promise in mitigating this problem. As reported by Ataee et al. [8], the stiffness of Ti6Al4V gyroid structures is comparable to the range of trabecular bone when the relative density ranges from 15 to 18%. Musthafa et al. [9] found that the compressive behaviour of TPMS structures is strongly linked to the design and geometric properties, suggesting that the stiffness can be lowered to approximate that of trabecular bone. Furthermore, the excellent fatigue properties of skeletal gyroid structures make them well-suited for cyclic physiological loading in vivo [10]. Given the complex physiological loading conditions, the design of gyroid structures for implants must consider their mechanical behaviour, particularly stiffness and failure mode.

Gyroid structures feature well-interconnected porosities, which facilitate body fluid flow and potentially enhance bone integration [11]. Hameed et al. [12] investigated gyroid structures with pore sizes ranging from 250 to 400 μm and found these structures to be biocompatible and conducive to stem cell adhesion and spread. To determine the pore and strut sizes, Walker et al. [13] proposed polynomial-fit-based formulas for calculation. Given the importance of relative density and pore size in mechanical properties and biomedical implant applications, it is essential to establish clear and accurate mathematical descriptions for these geometric properties. However, in most studies, the dimensions of geometric features, such as pore and strut size, are typically measured from samples or determined using statistical fits. To the authors' knowledge, explicit equations for precise control of these dimensions still lack investigation.

To deepen the understanding of gyroid structures for biomedical implants, an extended range of geometries is analysed to develop mathematical descriptions of the pores and strut sizes correlated with the definition parameters of gyroid structures. Additionally, both quasi-static compression tests and corresponding simulations are conducted to analyse the mechanical properties and identify the correlations between Young's modulus, yield stress, and relative density. Lastly, the deformation behaviour under different loading directions is investigated. The results of this research provide design information for the rapid determination of parameters in gyroid equations corresponding to specific geometric features. Furthermore, the findings concerning the deformation behaviour of gyroid structures contribute to expanding their potential applications in various fields.

2. Materials and Methods

2.1. Design and Geometric Characterisation of Gyroid Structures

The mathematical equation for gyroid structures was initially defined in 1970 [14] and is given by:

$$F(x, y, z) = cosx \cdot siny + cosy \cdot sinz + cosz \cdot sinx + C$$

where $x = \frac{2\pi X}{U}$, $y = \frac{2\pi Y}{U}$, $z = \frac{2\pi Z}{U}$, (X, Y, Z) represent the coordinates in 3D space. U denotes the unit cell size, and the variable C controls the relative density (volume fraction). A Matlab script was created to generate gyroid structures with various relative densities, unit cell sizes, and boundary sizes. The generated structures were then exported as STL files for further analysis.

Gyroid structures with different C values (−1.5 to 1.5) and unit cell sizes (1 to 4 mm) were created using the Matlab script for geometric property characterisations. These structures were then analysed using Siemens NX (version 2206, Siemens AG, Munich, Germany).

Figure 1a shows the definition of the pore core (green sphere), pore channel, and strut diameter. The geometric data were analysed using an R script [15]. An analytical analysis was performed to obtain the mathematically described geometric properties.

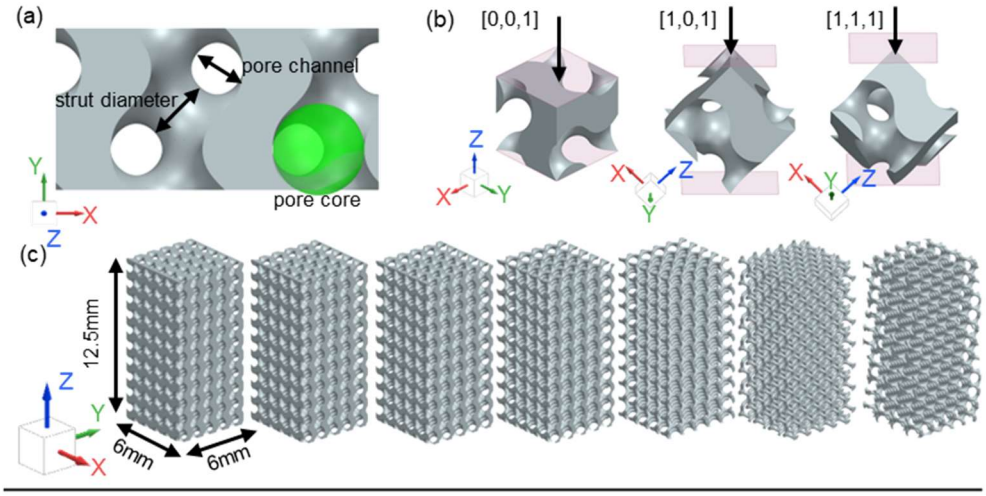

Unit cell size	1.2 mm						
C	0	0.3	0.5	0.8	1.1	1.1	1.1
ρ_{CAD}	50%	40.29%	33.77%	23.80%	13.42%	13.37%	13.33%
Loading direction	[0,0,1]	[0,0,1]	[0,0,1]	[0,0,1]	[0,0,1]	[1,0,1]	[1,1,1]

Figure 1. (**a**) Definition of pore core (green sphere), pore channel, and strut diameter in a two-unit structure. (**b**) Indications of different loading directions based on single units. (**c**) Gyroid structures for compression tests and simulations, with dimensions and loading directions indicated.

For simulation and compression testing, gyroid structures with a unit cell size of 1.2 mm were defined within a boundary volume measuring width = length = 6 mm and height = 12.5 mm (Figure 1c). Four different C values (0.3, 0.5, 0.8, and 1.1) were used for the structures in compression tests and five (0, 0.3, 0.5, 0.8, and 1.1) for simulations. The corresponding theoretical relative density (ρ_{CAD}) of the gyroid structures is presented in Figure 1c.

To investigate the effect of the loading direction on mechanical properties, gyroid structures with C = 1.1 were generated in three distinct orientations, i.e., the default orientation [0,0,1], a rotation along the Y-axis by −45° ([1,0,1]), and a further rotation along the X-axis by 45° ([1,1,1]); see Figure 1b,c.

2.2. Numerical Analysis of Compressive Behaviour of Gyroid Structures

Multistep nonlinear simulations were conducted using a Nastran solver to investigate the mechanical properties of gyroid structures under compressive loading. Gyroid structures of five relative densities (Figure 1c) and three loading directions (Figure 1b,c) were used. A dummy material with a Young's modulus of 110 GPa and a maximum stress of 1300 MPa was used to represent the LPBF-manufactured Ti6Al4V [16]. To determine the element size in simulations, a mesh sensitivity analysis was performed on a gyroid structure (unit cell size 1.2 mm, C = 0.3, ρ_{CAD} = 40.29%, length = width = 2.4 mm, height = 4.8 mm). The subsequent simulations employed quadratic tetrahedral meshes, with the mesh size equivalent to 40% of the strut diameter. Fixed constraints in the Z-axis were applied to the bottom surface of structures. A vertical load corresponding to 2.5% engineering strain was applied to the top surface.

The displacement and reaction force results were then converted into stress–strain curves, further determining the Young's modulus and yield stress of gyroid structures.

Subsequently, the obtained Young's modulus and yield stress values were fit into power relationships correlated with relative density.

The Gibson–Ashby correlation can be used to determine the Young's modulus of porous structures [17,18]. Researchers have reported that the Young's modulus and yield stress of gyroid structures are power correlated with relative density [19,20]:

$$\frac{E}{E_s} = a_1 \left(\frac{\rho}{\rho_s}\right)^{b_1}$$

$$\frac{\sigma_y}{\sigma_{ys}} = a_2 \left(\frac{\rho}{\rho_s}\right)^{b_2}$$

where E, σ_y, and ρ are Young's modulus, yield stress, and density of porous structures, respectively; E_s, σ_{ys}, and ρ_s are Young's modulus, yield stress, and density of solid matrix material, respectively; a_1, a_2, b_1, and b_2 are constants. The normalised Young's modulus and yield stress are defined as E/E_s and σ_y/σ_{ys}, respectively. The relative density (ρ_r) is defined as ρ/ρ_s.

2.3. Manufacturing of Gyroid Structures

A ProX 320B (3D Systems, Leuven, Belgium) LPBF machine was used to manufacture Ti6Al4V-ELI (grade 23, Carpenter Additive, Widnes, UK, particle size 15–53 μm) gyroid samples. Table 1 shows the process parameters employed in the LPBF process. Three specimens were manufactured for each structure. All specimens were then removed from the build plate using wire Electric Discharge Machining (EDM). Subsequently, the specimens underwent cyclic ultrasonic cleaning in water and ethanol to remove residual loose powder.

Table 1. Laser powder bed fusion (LPBF) parameters used in this study.

Laser parameters	Laser power	45 W
	Laser scan speed	300 mm/s
	Laser beam diameter	90 μm
Scan strategy	Layer height	30 μm
	Number of contours	1
	Contour offset	50 μm
	Fill offset	25 μm

The mass and dimensions of the specimens were measured to calculate their structural relative density (ρ_{sample}). The relative density of the struts (built volume) was measured based on Archimedes' principle. The volume of the struts in the gyroid structures was determined by immersing the samples in ethanol and measuring the weight difference in air and ethanol. This difference corresponds to the ethanol weight that occupies the same volume as the struts. Subsequently, the weight of the samples was divided by the measured volume of the struts to calculate their strut density. The relative density of struts is calculated using the density of solid Ti6Al4V (4.43 g/cm^3) as the reference. Three solid specimens, following the same procedures of manufacturing and postprocessing, were produced as the control group for compression tests.

2.4. Compression Test

Quasi-static compression tests were conducted using an Instron 3367 testing system (Instron, Norwood, MA, USA), with a preload of 50 N at a 0.5 mm/min rate. Subsequently, specimens were compressed at a constant engineering strain rate of 0.001 /s. During tests, the strain was continuously measured using the Video Extensometer (Instron AVE2, Instron, Norwood, MA, USA) and the deformation of the specimens was recorded using a 12M-pixel camera (IMX 603, Sony, Tokyo, Japan). The Young's modulus and yield stress for

each specimen were calculated based on the stress–strain curves in the compression test data, which were further fit into power relationships and compared with the correlations derived from simulations.

To enable the direct comparison of samples that experienced large deformation, the specific absorbed energy is limited to the strain of 30%:

$$W = \int_0^{0.3} \sigma(\varepsilon) d\varepsilon$$

where W is specific absorbed energy, σ and ε are engineering stress and strain during compression tests, respectively.

3. Results

3.1. Geometric Properties of Gyroid Structures

The relationship between the relative density of gyroid structures and the parameter C exhibits a linear correlation, Figure 2a. The relative density increases with lower C values, leading to thicker struts and smaller pores. A relative density of 50% corresponds to C being 0. C higher than 1.41 leads to non-continuous volumes, while C equals −1.5 generates fully dense structures. Neither struts nor pore channels are visible when C equals or undercuts −1. Examining the strut diameter, pore channel, and pore core sizes displayed as green spheres in Figure 2b–d, the values reveal linear proportionalities to the unit cell size when C falls within the −1 to 1 range. Consistent results were found for strut diameter, pore core, and pore channel sizes when comparing CAD measurements (green spheres) with explicit analytical results (red surfaces).

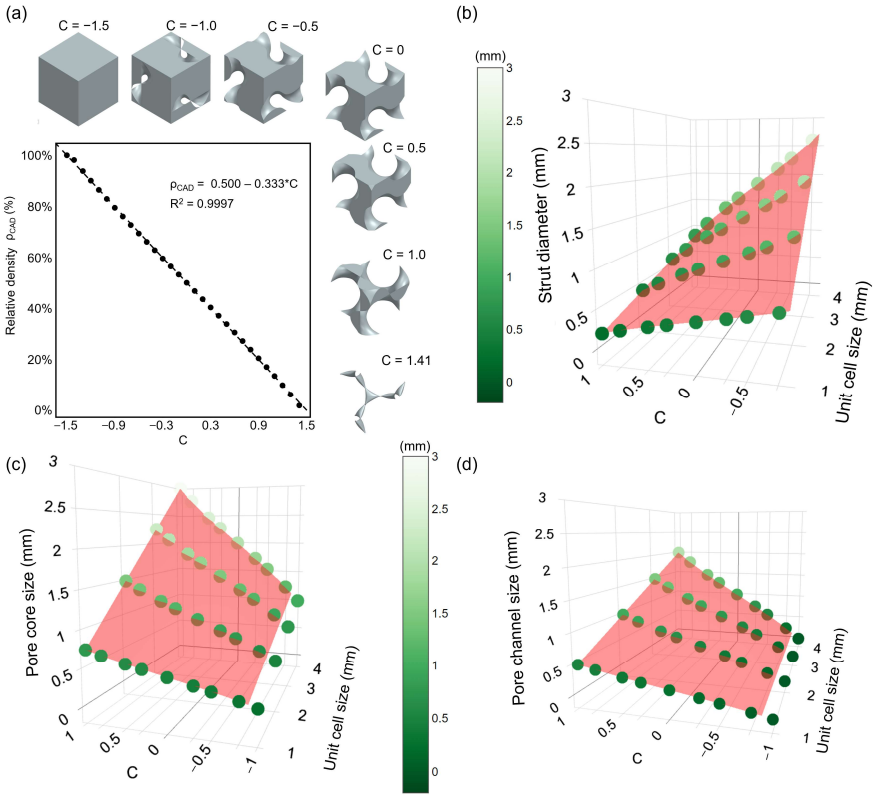

Figure 2. Geometric characterisations of gyroid structures. (**a**) Correlation between relative density and parameter C, with images of the gyroid unit for different C values. Correlations of strut diameter (**b**), pore channel (**c**), and pore core (**d**) with unit cell size U and parameter C. Green spheres represent the feature size measured from CAD models. The red surfaces represent analytical analysis results and can be described as equations by the end of Section 3.1. The detailed results of the geometric analysis can be found in the Supplementary Data.

Figure 3 shows the approach of analytical analysis on feature sizes in gyroid structures. Given the continuous repeating units in gyroid structures, the pore core, pore channel, and strut can be calculated from specific line sections (L_1 to L_4) using the following equations:

$$Pore\ core = L_1 + L_4$$

$$Pore\ channel = 2L_4$$

$$Strut\ diameter = \sqrt{2}\frac{U}{2} - 2L_4$$

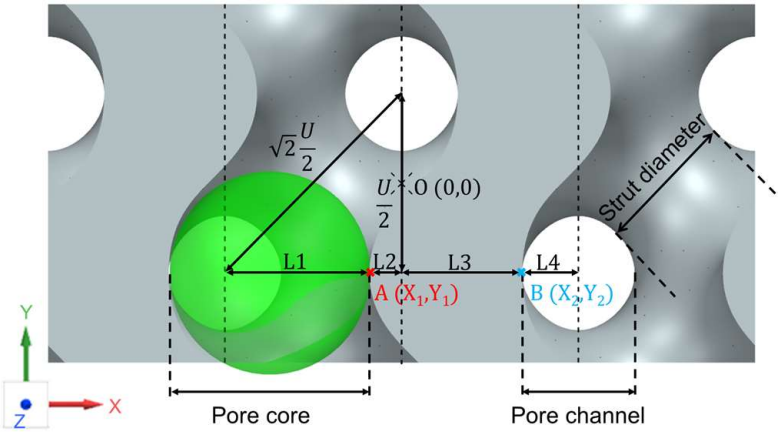

Figure 3. Schematic representation of calculating the geometric feature sizes using the analytical approach in a two-unit gyroid structure. The dimensions of this structure are 2 units in X, 1 unit in Y and Z. The centre of the image is defined as the 0 point.

The length of these line sections can be determined by calculating the X coordinates of two points on the gyroid surface (A and B). The gyroid surface equation can be rewritten as

$$F(x,y,z) = cos\frac{2\pi X}{U} \cdot sin\frac{2\pi Y}{U} + cos\frac{2\pi Y}{U} \cdot sin\frac{2\pi Z}{U} + cos\frac{2\pi Z}{U} \cdot sin\frac{2\pi X}{U} + C$$

with $(X,\ Y,\ Z)$ representing the point coordinates in 3D space. X_1 and X_2 can be calculated by setting $Y = -\frac{U}{4}$ (the Y value of line sections L_1 to L_4) and $Z = \frac{U}{2}$ (the front surface in Figure 3). The gyroid surface equation is then simplified as:

$$-\cos\left(\frac{2\pi X}{U}\right) - \sin\left(\frac{2\pi X}{U}\right) + C = 0$$

When C ranges between -1 and 1, the solution for X is:

$$X = \frac{U(\tan^{-1}\left(\frac{1\pm\sqrt{2-C^2}}{C+1}\right) + \pi n)}{\pi}, when\ C+1 \neq 1\ and\ n \in Z$$

Considering πn is repeating in 3D space, the solution can be further simplified as:

$$X_1 = \frac{U(\tan^{-1}\left(\frac{1-\sqrt{2-C^2}}{C+1}\right))}{\pi}, X_2 = \frac{U(\tan^{-1}\left(\frac{1+\sqrt{2-C^2}}{C+1}\right))}{\pi}$$

The line sections can be calculated from X_1 and X_2:

$$L_1 = \frac{U}{2} + X_1, L_2 = -X_1,\ L_3 = X_2,\ L_4 = \frac{U}{2} - X_2$$

The geometric features can be determined as follows:

$$Pore\ core = L_1 + L_4 = U + X_1 - X_2 = U + \frac{U\left(\tan^{-1}\left(\frac{1-\sqrt{2-C^2}}{C+1}\right)\right)}{\pi} - \frac{U\left(\tan^{-1}\left(\frac{1+\sqrt{2-C^2}}{C+1}\right)\right)}{\pi};$$

$$Pore\ channel = 2L_4 = U - \frac{2U\left(\tan^{-1}\left(\frac{1+\sqrt{2-C^2}}{C+1}\right)\right)}{\pi};$$

$$Strut\ diameter = \sqrt{2}\frac{U}{2} - 2L_4 = \sqrt{2}\frac{U}{2} - U + \frac{2U\left(\tan^{-1}\left(\frac{1+\sqrt{2-C^2}}{C+1}\right)\right)}{\pi};$$

The analytical results of strut diameter, pore channel, and pore core sizes are visualised as red surfaces in Figure 2b–d.

3.2. Uniaxial Compressive Behaviour of Gyroid Structures Through Simulation

Figure 4 shows the results of the mesh sensitivity analysis. The convergence of Young's modulus, indicated by a less than 1% difference between results, is achieved when the element size of the structures is 40% of the strut diameter or less.

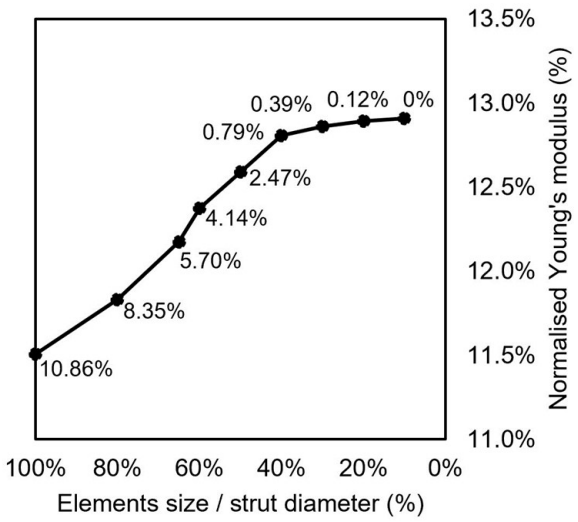

Figure 4. Results of mesh sensitivity analysis based on Young's modulus. Differences between the results for various element sizes and the final values (element size = 10% of strut diameter) are indicated next to the marks.

Figure 5a,b illustrate the stress and strain distributions within gyroid structures at 1% overall strain. Notably, stress and strain concentrations in structures loaded in the [0,0,1] direction appear at a 45° angle relative to the loading direction. The stress concentrations increase with relative density, as indicated by higher stress values in the concentrated regions. Stress and strain also concentrate on the thin features of the structure boundaries (surfaces). The influence of loading direction on stress and strain distribution is evident in the three structures with C = 1.1. In structures loaded in the [1,0,1] direction, stress and strain are concentrated in the middle of horizontal and vertical struts, whereas the concentration in structures loaded in the [1,1,1] direction appears in the middle of struts oriented at nearly 45°. Furthermore, strain concentration areas indicate the potential failure points or zones prone to deformation, highlighting critical regions that could lead to structural instability under further loading.

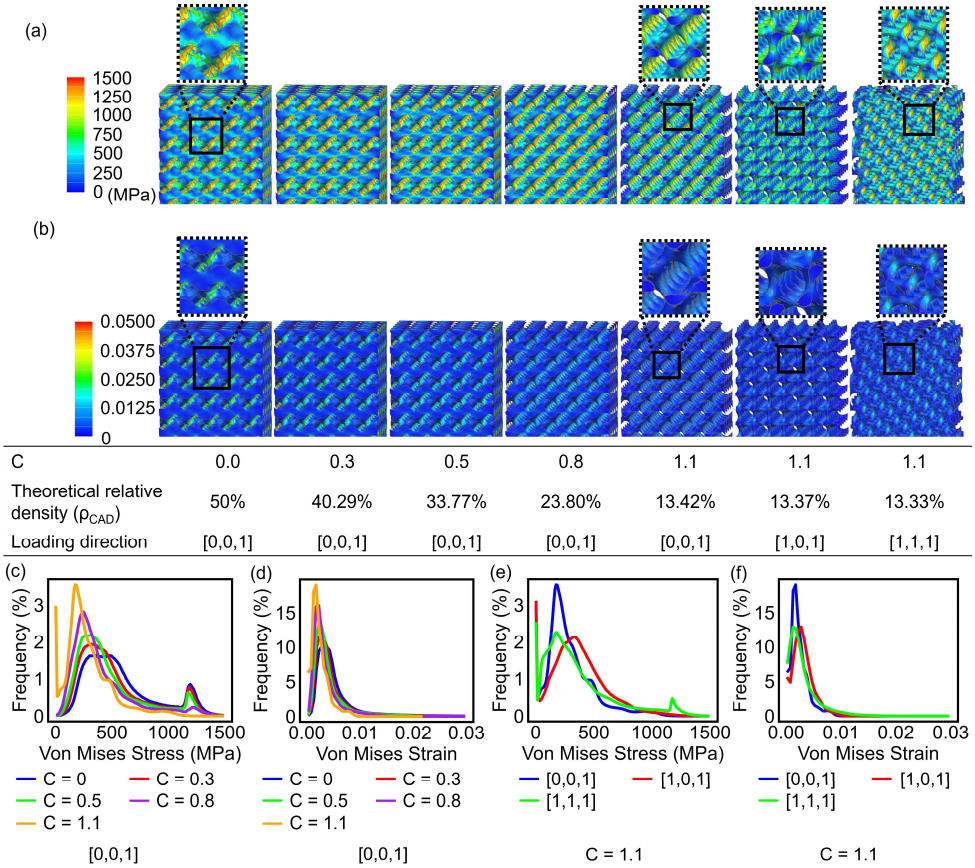

Figure 5. Simulation results of stress distributions (**a**) and strain distribution (**b**) in gyroid structures at 1% overall strain (before yield), with indications of parameter C, relative density, and loading direction. Higher magnification of stress and strain distributions are shown. Corresponding histograms are shown for stress (**c**) and strain (**d**) in gyroid structures with varying relative density (loading direction [0,0,1]), and stress (**e**) and strain (**f**) in gyroid structures with different loading directions (C = 1.1).

The histograms in Figure 5c to f further illustrate these patterns. In structures loaded in the [0,0,1] direction, stress and strain shift towards higher values with increased relative density (lower C). When comparing the three loading directions in the range of high stress (over 1000 MPa) and strain (over 0.01), the structure loaded in the [1,1,1] direction exhibited the highest values, while the structures loaded in the [0,0,1] direction showed the lowest values. Furthermore, similar to the denser structures, the structure loaded in the [1,1,1] direction displayed a stress peak at around 1200 MPa in its stress distribution histogram (Figure 5d).

The coloured curves in Figure 6 present the stress–strain curves derived from simulation results. All structures demonstrated linear elastic sections, yield, and stress-hardening in the curves. In the comparison of relative densities (Figure 6a), porous structures exhibit lower stress values and flatter slopes in the linear elastic sections. When comparing the linear sections in curves of different loading directions, the structure loaded in the [1,1,1] direction showed the highest stress and slope, while the [0,0,1] direction exhibited the lowest (Figure 6b). Table 2 includes the simulation results of Young's modulus and yield, both of which show a positive correlation with relative density.

Table 2. Properties of gyroid structure in simulations and compression tests.

C	Loading Direction	Theoretical Relative Density (ρ_{CAD})	Young's Modulus (Simulation)	Yield Stress (Simulation)	Relative Density of the Samples (ρ_{sample})	Relative Density of the Struts	Young's Modulus (Test)	Yield Stress (Test)	Maximum Stress (Test)	Strain at First Maximum Stress (Test)	Specific Absorbed Energy (Test)
Unit	**-**	**[%]**	**[GPa]**	**[MPa]**	**[%]**	**[%]**	**[GPa]**	**[MPa]**	**[MPa]**	**[%]**	**[MJ/m^3]**
control	-	100	110	1150	99.53 ± 0.12	-	78.88 ± 3.19	979.59 ± 2.07	1370.67 ± 13.38	16.41 ± 0.25	195.01 ± 4.52
0	[0,0,1]	50.00	22.85	199.99	-	-	-	-	-	-	-
0.3	[0,0,1]	40.29	14.07	131.33	41.69 ± 0.14	98.96 ± 0.06	12.25 ± 0.06	136.68 ± 0.67	191.54 ± 1.37	6.07 ± 0.15	46.62 ± 4.87
0.5	[0,0,1]	33.77	9.47	94.80	35.30 ± 0.21	99.17 ± 0.22	7.99 ± 0.56	94.75 ± 4.09	136.70 ± 0.56	6.46 ± 0.06	34.44 ± 0.40
0.8	[0,0,1]	23.80	4.27	50.86	25.72 ± 0.18	99.20 ± 0.14	3.72 ± 0.04	52.93 ± 1.09	75.81 ± 0.32	6.30 ± 0.17	19.00 ± 0.23
1.1	[0,0,1]	13.42	1.15	20.12	15.46 ± 0.17	99.31 ± 0.16	1.30 ± 0.01	20.44 ± 0.42	29.58 ± 0.31	6.26 ± 0.14	6.87 ± 0.10
1.1	[1,0,1]	13.37	1.85	31.19	15.19 ± 0.19	99.33 ± 0.26	2.18 ± 0.05	28.78 ± 0.41	37.27 ± 0.57	3.64 ± 0.48	7.49 ± 0.10
1.1	[1,1,1]	13.33	2.31	26.37	15.97 ± 0.02	99.28 ± 0.25	2.03 ± 0.08	25.11 ± 0.11	34.39 ± 0.82	4.36 ± 0.42	7.71 ± 0.11

Young's modulus and yield stress derived from simulation results are power correlated with relative density, Figure 7. These power relationships demonstrate high R^2 values, yet they differ from the results reported by Gibson–Ashby [18] and Yan et al. [20].

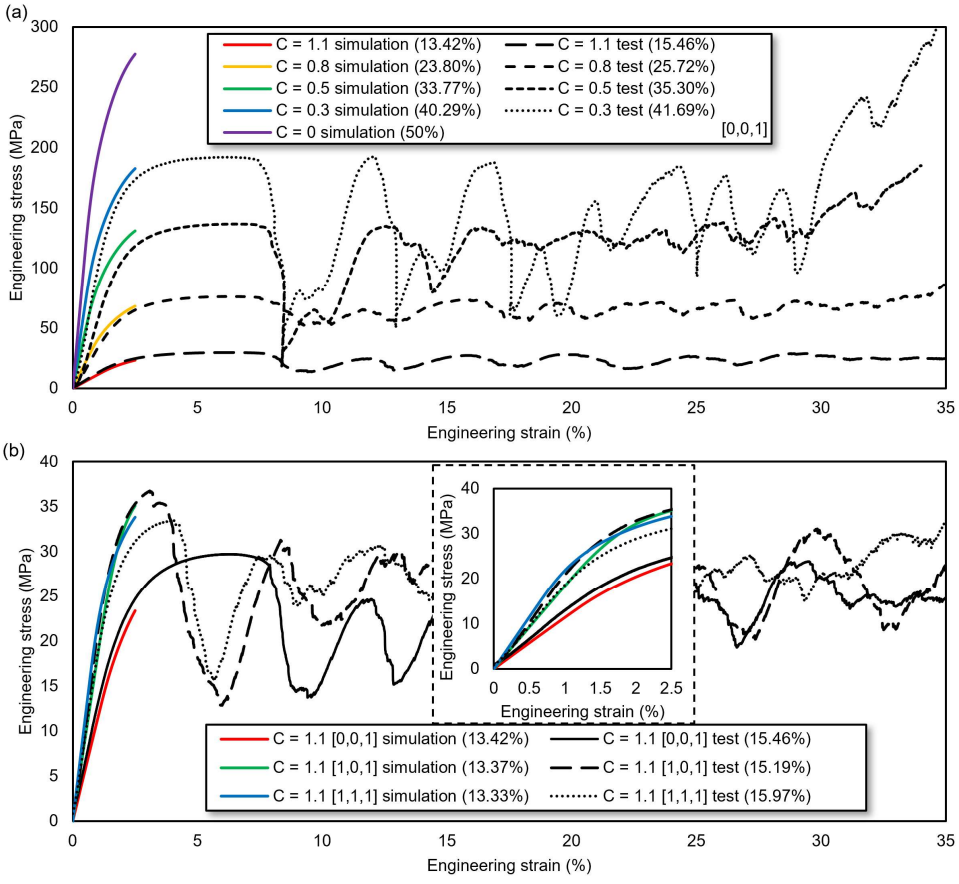

Figure 6. Comparison of stress–strain curves of gyroid structures with (**a**) different relative density (loading direction [0,0,1]) and (**b**) loading directions (C = 1.1). Loading directions are indicated in square brackets. The corresponding ρ_{CAD} and the average ρ_{sample} are shown in round brackets.

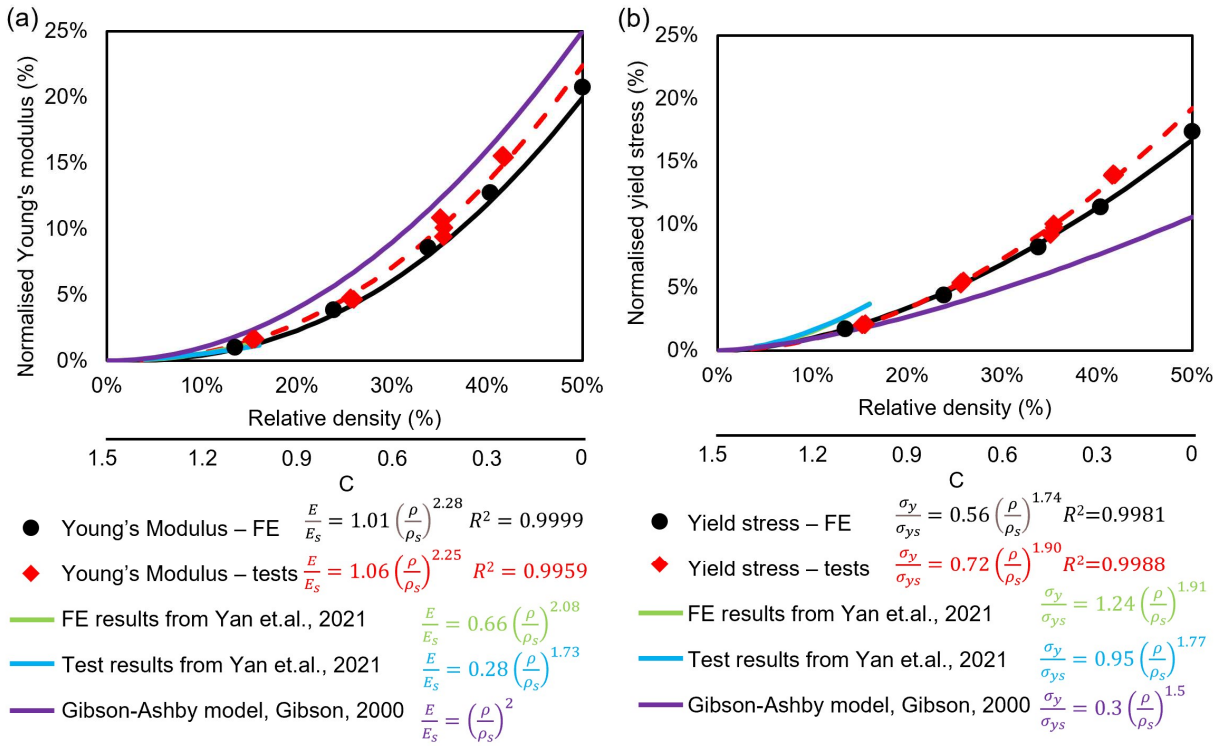

Figure 7. (**a**) Power relationships between normalised Young's modulus and relative density of gyroid structures. (**b**) Power relationships between normalised yield stress and relative density of gyroid structures. Structures are loaded in the [0,0,1] direction. The theoretical relative density (ρ_{CAD}) was used to represent data in simulations, and the measured relative density (ρ_{sample}) was used to illustrate data in tests. The power relationships are compared with the work of Yan et al. [20] and the Gibson–Ashby [18] model.

3.3. Verification of Mechanical Behaviour for Gyroid Structures Through Compression Tests

Figure 8 shows the optical microscope images of samples after LPBF manufacturing; a large number of adherent particles are visible, indicating a slight overbuild. Table 2 presents the measured relative density (ρ_{sample}) of samples. Notably, all samples demonstrated a higher relative density than their theoretical values, with most samples exhibiting a relative density of struts exceeding 99%.

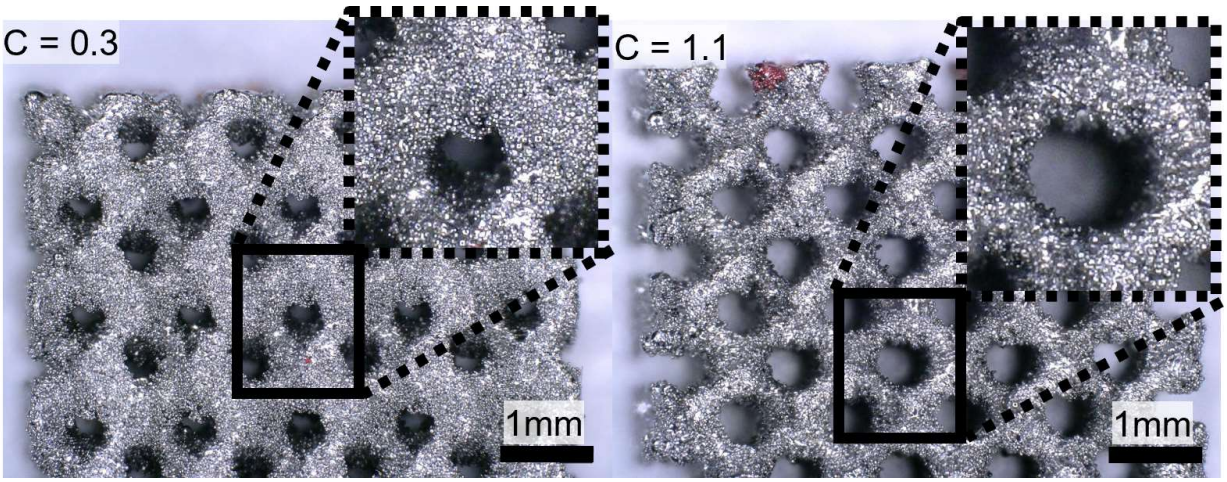

Figure 8. Optical microscope images of as produced samples.

Figure 6a shows the stress–strain curves obtained from the quasi-static compression tests of samples with different relative densities. The gyroid structures in the compression tests exhibited curves similar to simulation results up to a strain of 2.5%, exhibiting linear elastic sections, yield, and strain-hardening stages. Dense structures demonstrated higher Young's modulus and yield stress than porous structures. Initial fractures of all samples loaded in the [0,0,1] direction occurred at a strain of approximately 8%. Table 2 presents the relative density and mechanical properties of gyroid samples in the compression tests. Among the structures loaded in the [0,0,1] direction, Young's modulus, yield stress, maximum stress, and specific absorbed energy exhibit positive correlations with relative density. In these structures, the strain at the first maximum stress is approximately between 6% and 6.5%. However, the two structures loaded in different directions display higher Young's modulus, yield stress, maximum stress, lower strain at first maximum stress, and comparable specific energy (Figure 6b and Table 2). Compared to the structures loaded in the [0,0,1] direction, the structures loaded in the [1,0,1] and [1,1,1] directions showed earlier initial fractures at higher stress, along with greater differences in the stress–strain curves of simulations and tests. Nevertheless, plateau regions, seen as fluctuating stress over large strain ranges, were identified after initial failure in all samples. Increased stress due to structural densification was observed towards the end of the test. The impact of relative density and loading direction on mechanical properties will be further discussed in Sections 4.2 and 4.3.

Table 3 further confirms the variation in Young's modulus when the gyroid structures were subjected to different loading directions. The simulation results indicate the highest Young's modulus in the [1,1,1] direction and the lowest values in the [0,0,1] direction, aligning with the findings of Yan et al. [20]. However, the Young's modulus derived from tests exhibits higher values and demonstrates a different pattern across loading directions. Unlike the simulation results where the structures loaded in the [1,1,1] direction have the highest Young's modulus, the structures loaded in the [1,0,1] direction display the greatest stiffness in tests.

Table 3. Comparison of normalised Young's modulus in this study and calculated values based on the same relative density (ρ_{CAD}) from Yan et al. [20].

C	Loading Direction	Result of This Study		Yan et al. [20]
		Simulation	Test	FE
1.1	[0,0,1]	1.05%	1.65 ± 0.02%	1.12%
	[1,0,1]	1.68%	2.76 ± 0.06%	1.56%
	[1,1,1]	2.10%	2.57 ± 0.10%	2.10%

Table 4 details the progressive failures observed in gyroid structures during compression tests. Most specimens exhibited concentrated initial failures at approximately 45° relative to the loading direction, followed by progressive failures and eventual densification. Dense structures (C = 0.3) underwent horizontal shifts while porous structures (C = 1.1) experienced densification with vertical stacking post-failure. During deformation, struts bent, fractured, and gradually contacted each other, indicating a bending-dominant deformation and failure mode. The initial fracture locations in struts corresponded to stress and strain concentrations. Specifically, failures in the structures loaded in the [0,0,1] direction initiated from the 45°-oriented struts, while in the structures loaded in the [1,0,1] direction, failures initialised in the middle of struts. Conversely, in the structures loaded in the [1,1,1] direction, failure involved the bending of numerous 45°-oriented struts.

Table 4. Deformation and failure mode of gyroid samples during compression tests.

C	ρ_{sample} (%)	Loading Direction	Strain (ε, %)				
0.3	41.69 ± 0.14	[0,0,1]	0	1.5	11.1	20.4	34.0
					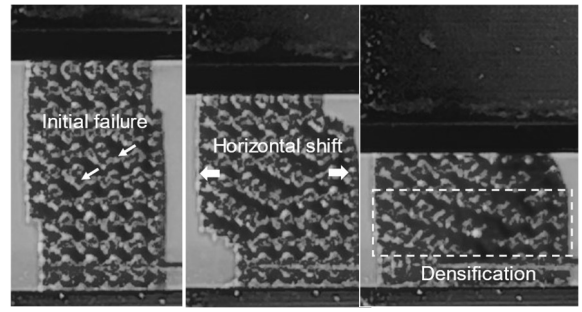		
1.1	15.46 ± 0.17	[0,0,1]	0	1.8	11.8	20.4	38.0
					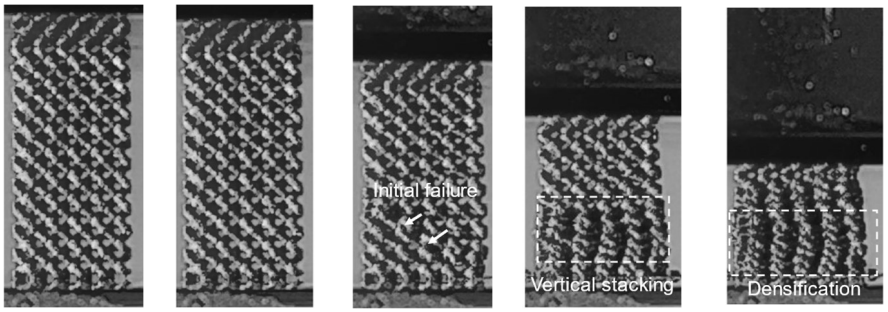		
1.1	15.19 ± 0.19	[1,0,1]	0	2.3	14.8	30.0	37.0
					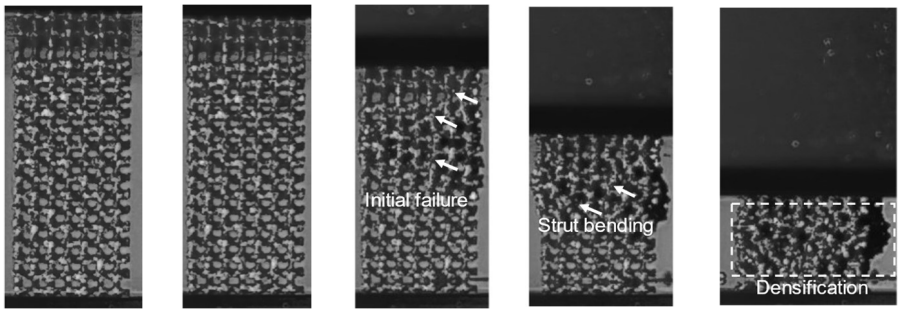		
1.1	15.97 ± 0.02	[1,1,1]	0	2.4	11.1	24.6	40.0
					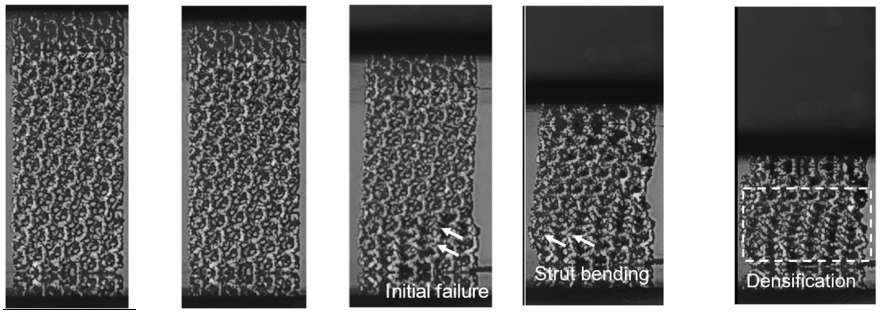		

4. Discussion

4.1. Adaptive Geometric Properties

The geometric properties of gyroid structures are strongly associated with the parameter C and the unit cell size. The observed linear relationship between relative density and C aligns with the findings of other researchers [2,21]. Higher C values decrease the relative density of gyroid structures, leading to thinner struts and larger pores. Maintaining a continuous volume within the porous gyroid structure typically requires a C value ranging

from −1.5 to 1.41. Pore channels and struts are not visible in gyroid structures with C values lower than −1.0, thus falling within the applicable C value range of −1.0 to 1.41. In any case, pore and strut sizes follow the analytical relationship within the C value range of −1.0 to 1.0. With a fixed C value, gyroid structures with varying unit cell sizes maintain identical geometries, with their dimensions scaling proportionally. Consequently, strut diameter, pore channel, and pore core sizes exhibit linear correlations with the unit cell size, as evidenced by both CAD measurements and explicit analyses. These explicit equations facilitate precise control over geometric features, enabling rapid determination of design parameters (unit cell size and C) to generate gyroid structures with specific relative density, pore size, and strut diameter.

The high porosity of gyroid structures holds promise for biomedical orthopaedic implant applications, offering enhanced osseointegration and improved implant stability. The continuous and non-angular TPMS sustains an ideal environment for cell attachment and proliferation [3]. Pores are crucial in facilitating these cellular activities [22]. Interconnected pores allow fluid flow, promoting nutrient and oxygen supply for cells [23,24]. Porous materials with a relative density below 50% [23,25,26] and pores sizes ranging from 100 to 700 μm [22,27] have demonstrated considerable potential for osseointegration. The correlations derived from this geometric analysis guide the determination of suitable ranges for C and unit cell size to generate gyroid structures with high potential in osseointegration, particularly by selecting C values greater than 0 and using specific combinations of C and unit cell size.

4.2. The Effect of Relative Density on Compressive Behaviours

In general, the employed LPBF process parameters ensured satisfactory manufacturing quality of the samples. The high relative densities of the struts confirm the low ratios of porosity defects. Yet, the slightly higher relative density (ρ_{sample}) observed in samples is usually characterised as overprinting, due to heat input during the process. The additional heat inevitably affects the material adjacent to the built volume. Consequently, particles may adhere to the sample surface, increasing both built volume and relative density.

The stress and strain distributions in simulations reveal the deformation behaviour of gyroid structures under compressive load. Struts in gyroid structures experience a combination of bending and compression deformation, with bending being the main cause of stress concentration and subsequent failures [10,28]. Stress and strain concentration predominantly occur on struts oriented at a 45° angle relative to the loading direction, corresponding to the direction of the maximum shear stress. The histograms reflect the intense stress concentrations in dense structures. Most materials experience low stresses, seen as the high-frequency peaks at lower stress ranges. In contrast, the material on 45° orientated features experiences higher stress and displays low-frequency peaks at higher stress ranges. At equal engineering strain, the stress concentration is more pronounced in dense structures, attributed to their higher stiffness. The observations suggest that increased relative density leads to greater stress concentration within the structures, which aligns with the findings reported by Yang et al. [10]. Stress concentration approaches the yield stress of Ti6Al4V, implying the initial failure locations at stress concentrations. The thin features on the boundary surfaces of the structures caused unfavourable stress and strain concentrations. These locations are highly susceptible to initial failures, potentially leading to numerous sharp edges and ends that could pose risks in biomedical applications. Hence, implant designs should aim to minimise or avoid such thin features.

The stress–strain curves illustrate distinct deformation behaviours of gyroid structures with varying relative densities. In general, denser structures showed higher stress values due to their high stiffness. Both simulation and test curves consistently demonstrate the linear elastic sections and yield, confirming that the material model used in simulations can represent the linear elastic deformation and yield of LPBF-manufactured Ti6Al4V. However, the maximum deformation in simulations is restricted to strain = 2.5% due to software limits, resulting in the exclusion of plateau regions in the simulation curves. Discrepancies

between simulation and test curves can be attributed to using a simplified material model in simulations. Furthermore, the wide plateau regions in tests consist of stress peaks and valleys over a large strain range, resulting from local collapse and regained support during continuous deformation. The periodic changes of stress over deformation align with the observation by Fan et al. [29]. This implies the good deformability of gyroid structures during progressive failures, aligning well with their application as energy absorbers.

The deformation behaviours and failure modes of gyroid structures are strongly influenced by relative density. In the structures loaded in the [0,0,1] direction, stress typically concentrates at thin features or sharp corners. Due to the period geometry of gyroid structures, its cross-section reaches the minimum area at 45° with respect to the loading direction [29], corresponding to a weak orientation prone to failures primarily induced by the shear load [30]. The failure manifests as bending, plastic deformation, and fractures of the struts. The relatively thicker features in dense structures enhance local stiffness, enabling the failure and defect accumulations near initial cracks. The high stiffness also ensures that the resilient volume can support the fragments during progressive failure, seen as fragments of dense structures that horizontally shifted after initial fractures. Thus, the dense structures showed 45° diagonal fractures. Conversely, the low stiffness associated with thin struts in porous structures results in localised failure initiation. Throughout the compression tests, the low stiffness of the material cannot horizontally shift the fragments. Thus, the deformed volume in porous structures tends to stack vertically, causing layer-by-layer failures and gradual densifications.

The power relationships of Young's modulus and yield stress show notable consistency between simulation and test results, affirming the robustness of both approaches. The slight difference can be attributed to inherent manufacturing defects within the LPBF process and the slight increase in dimensions and relative density of specimens. Transitioning to a comparison with existing literature, divergence from the power relationships proposed by Gibson–Ashby [18] is understandable, given their use of metallic foam, a porous material distinct from the skeletal gyroid structure. Larger disparities with the work of Yan et al. [20] can be attributed to their focus on more porous gyroid structures with a narrow relative density range (5% to 15%). This limitation can narrow the applicability of formulas that are intended to describe mechanical properties across the entire relative density range.

The power relationships of Young's modulus and yield stress offer high customisability in various applications. By selecting appropriate C values corresponding to the desired relative density, gyroid structures with precise Young's modulus can be accurately generated. This variability highlights the excellent potential of gyroid structures in biomedical implants, where stiffness can be tailored to align with the value of human bone (typically around 20 GPa or lower [31]). As demonstrated in [32], low-stiffness porous materials can be used to replace the volume of stiff metal stem components in artificial joints, thereby reducing the overall stiffness of the stem and allowing the bone to be stimulated to maintain its integrity. Based on the results of this study, gyroid structures with C = 0 achieves a stiffness of approximately 20 GPa. This geometric configuration presents a promising solution for reducing the stress-shielding effect. Similar adaptive mechanical properties are observed in various porous materials, which further explores the range of porous materials for biomedical applications [33].

4.3. The Effect of Loading Direction on Compressive Behaviour and Anisotropy

The stress distribution of gyroid structures reflects the loading conditions of the struts. In lattice structures, the struts aligned with the loading direction primarily experience compression during deformation while lateral struts undergo stretching [34]. By using the approach proposed by Yang et al. [19], gyroid structures can be simplified as scaffolds of cylindrical struts, allowing for the computational determination of strut orientations using line beam data. The unique shapes of gyroid lattice structures result in struts orienting across a wide spectrum of angles, see Figure 9. Therefore, struts experience a combination of bending and compression due to this diverse range of orientations. Comparisons of

stress distribution (Figure 5e) reveal significant stress concentration in structures loaded in the [1,0,1] and [1,1,1] directions. In the stress range over 1000 MPa and the strain range higher than 0.01, the structures loaded in the [1,1,1] direction consistently display the highest concentration, followed by the structures loaded in the [1,0,1] direction and [0,0,1] direction. Young's modulus in the simulation results of these three structures follows the same sequence (Table 3). This correspondence between stress concentration and stiffness is consistent with the findings from numerical analysis of the structures loaded in the [0,0,1] direction, indicating that stiffer structures demonstrate more pronounced stress concentrations under uniform compressive strain.

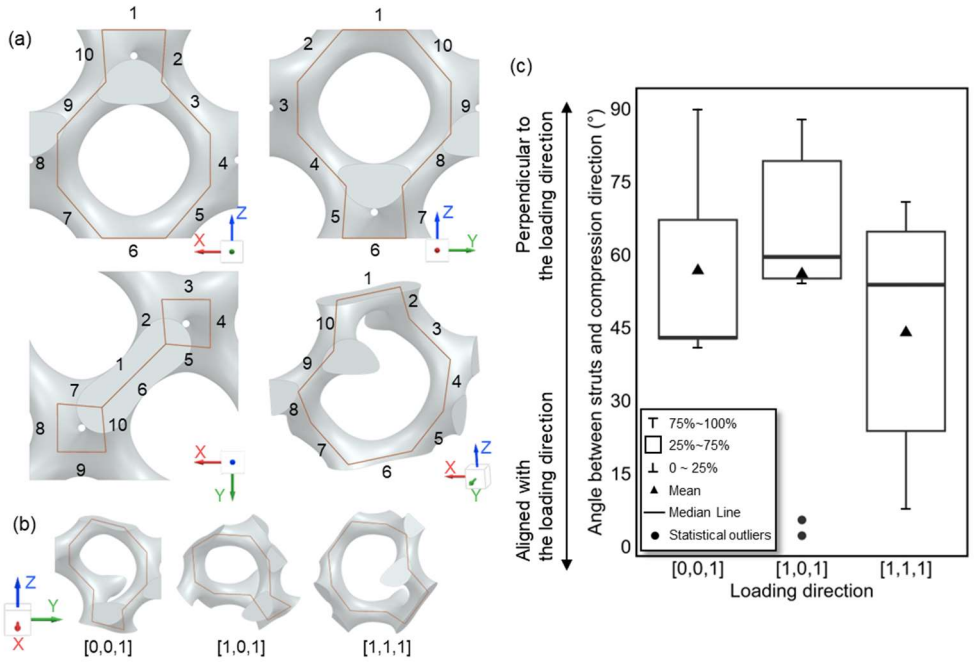

Figure 9. Struts orientation analysis of gyroid unit cell with parameter C = 1.1. (**a**) Schematics of gyroid units in different perspectives. The grey colour represents solid volume and the orange line beams represent the simplified struts. Corresponding labels for struts are shown. (**b**) Schematics of gyroid units in different loading directions. (**c**) The strut orientation for different loading directions, shown as the angle between struts and compression direction (Z-axis).

The mechanical response of gyroid structures changes with loading directions due to the varied strut orientations and distinct load transfer modes. Under compression, the load traverses through the lattice geometry towards the bottom of the structures, with the efficiency of this transfer influenced by the structure's geometry and strut orientation. Cuadrado et al. [35] compared the mechanical properties of lattice structures with different unit cells. Their results showed that as the inclination angle between struts and the loading direction increases, the deformation mechanism transfers from compression-dominant to bending-dominant, consequently reducing mechanical properties. The comparison of strut orientation in gyroid structures (Figure 9) reveals that struts in the structures loaded in the [0,0,1] direction are aligned at larger angles with the loading direction, indicating more bending-dominant behaviour. When the structure is loaded in the [1,0,1] direction, some struts align closely with the loading direction, thereby enhancing the stiffness. However, most struts remain inclined, which restricts the stiffness. Compared to the other two directions, the [1,1,1] direction exhibits the greatest number of struts closely aligned with the compression direction. As a result, the deformation mechanism approximates a compression-dominant behaviour, leading to the highest observed stiffness in the simulation results. This direction-specific stiffness underscores the inherent anisotropy of gyroid structures.

The stress–strain curves also elucidate the influence of loading directions on the mechanical response of gyroid structures. Structures loaded in the [1,0,1] and [0,0,1] directions exhibit increased stiffness and a decreased strain at initial fractures during testing. In these structures, local stress reaches the yield point at a lower strain. In the subsequent plastic deformation, defects such as dislocations, micro-cracks, and grain boundary separations rapidly accumulate at significant strain concentration locations, leading to fractures at lower strains. The increased stiffness observed in these two loading directions is accompanied by corresponding low strain at initial fractures. However, their superior deformability remains unaffected, as evidenced by wide plateau regions and comparable absorbed energy.

The mechanical properties of lattice structures are also highly dependent on the manufacturing process. The broad range of strut orientations presents challenges to the LPBF process. Overhangs can occur when struts align more closely with the build plate. Without a sufficient solid substrate, the new layer of materials in the overhang regions is prone to increased spattering. This results in less solid deposition, increasing defects such as material loss and high surface roughness [36]. Kranz et al. [37] discovered that struts more parallel to the build plate tend to induce defects such as high surface roughness and dimensional inaccuracies. Shange et al. [38] reported increased porosity when features align more closely with the build plates. These defects ultimately compromise the mechanical properties, reducing stiffness and deformability. Therefore, the support ratio of the LPBF process, defined as the proportion of the material layer supported by the previous layer, could indicate manufacturing quality. Figure 10 compares the material layers for manufacturing gyroid structures in three loading directions, revealing significant differences in sequential layer shapes for the three loading directions, associated with different support ratios. To further quantify the support ratios, the CAD models of the structures, oriented in three loading directions, were sectioned using the layer height of the LPBF process. These section images were then compared to calculate support ratios between layers; see Figure 11. Notably, the 2D geometries of the slices used in this analysis are identical to those used in generating laser trajectories.

The Young's modulus in compression tests exhibited higher values than those from the simulation results (Table 3). This increase can be attributed to the slightly higher relative densities (overbuild) of the produced gyroid structures (see Figure 8). Despite the consistent power relationships of Young's modulus in tests and simulations, discrepancies emerge for different loading directions. Structures loaded in the [1,0,1] direction demonstrate significantly higher stiffness in tests than the other two loading directions, which can be attributed to the improved manufacturing quality. Figure 11c illustrates the support ratios of the material layers when structures are produced and loaded in three directions. Among these, the [1,0,1] direction exhibits the highest support ratio. Consequently, this direction is expected to have the fewest overhangs and thus the least manufacturing defects. This results in an improved load-bearing capacity for this loading direction, leading to a higher Young's modulus. In contrast, the relatively low support ratios in the other two directions increase manufacturing defects and reduce Young's modulus, as evidenced in Table 3. Defects, such as porosity, can be significantly reduced by optimising laser parameters and scan strategies in the LPBF process, including adjustments to laser power and scan strategy, as demonstrated in a previous work of the authors [39].

The failure modes of gyroid structures under the three loading directions correspond to the stress concentrations observed in simulations. The initial failure locations of structures align with the strain concentration, specifically in the middle of struts where stress and strain concentrations are highest. The struts that align more closely with the loading direction, particularly in the [1,0,1] and [1,1,1] directions, exhibit a compression-dominant deformation. However, given the wide range of strut orientations, most struts display a bending-dominant deformation mechanism. The primary failure mode in gyroid structures involves the bending and rotation of struts, indicating a bending-dominant behaviour. During the progressive failure, deformed and failed struts stacked together due to the low

stiffness of the porous structures (with a relative density of around 15%) were unable to support the resilient volume.

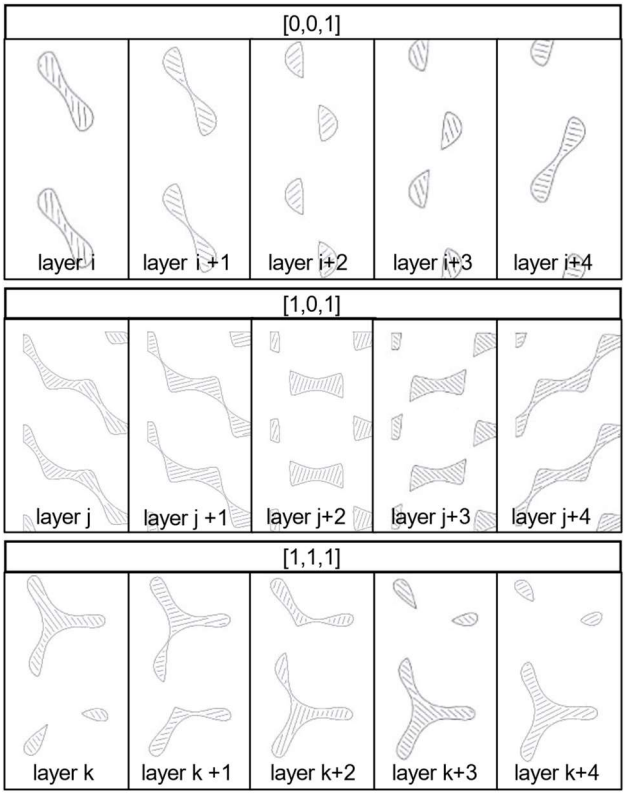

Figure 10. Detailed view of sequential building layers in slicing gyroid structures for three loading directions. Parameter C = 1.1.

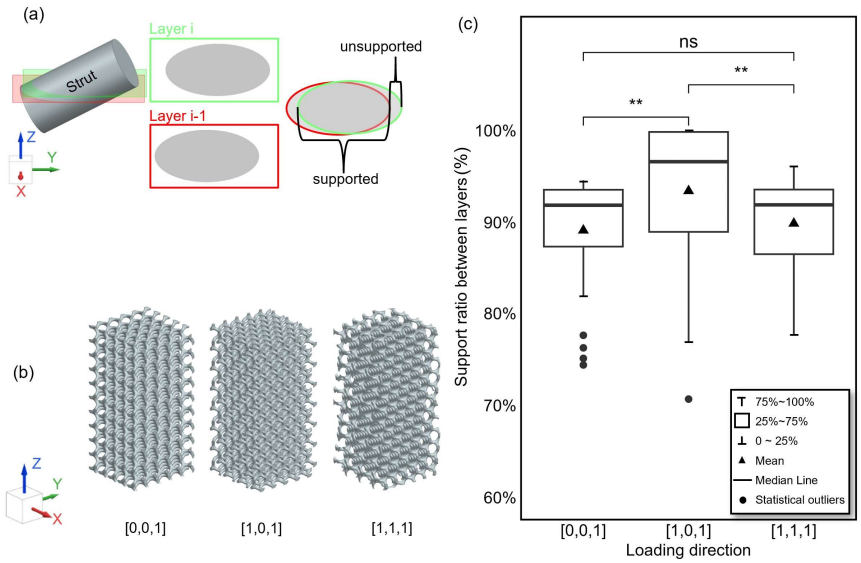

Figure 11. (**a**) Schematic of the principle of calculating the support ratio of material layers. (**b**) CAD models of gyroid structures in FEM analysis and compression tests, corresponding to Figure 1c. (**c**) Box plots of support ratios of gyroid structures in three loading directions. Comparisons show different significance codes. *p*-values ranges: 0.001 < ** < 0.01, 0.05 < ns (not significant).

The loading direction-dependent mechanical properties confirm the anisotropy of gyroid structures and expand the design possibilities for tailoring these structures to specific applications. In instances where a structure meets geometric parameter requirements,

such as pore sizes, but requires increased stiffness, optimising the orientation of the gyroid structure can be an effective design strategy. Moreover, the flexibility and potential of gyroid structures can be significantly enhanced when integrated with a graded structure design. The radial gradient design, as demonstrated in [21], is a promising approach to expanding the design possibilities of graded structures for enhancing mechanical performance and biological integration. For orthopaedic implants, the surface of an implant can be substituted with finely tuned gyroid structures exhibiting non-uniform stiffness and pore size. Consequently, the stress distribution at the bone interface can be customised to more effectively mitigate the stress-shielding effect, and the osseointegration process can be improved by applying an appropriate pore size.

5. Conclusions

This study investigated the geometric characteristics and the quasi-static compressive behaviour of skeletal gyroid structures. The key findings highlight the explicit description and control of gyroid structure geometries by adjusting parameters in mathematical definitions. The results demonstrated that increasing relative density elevates both Young's modulus and yield stress. Moreover, this study revealed the anisotropic behaviour of gyroid structures under various loading directions.

The relative density of gyroid structures exhibits a linear correlation with the parameter C. Pore size and strut diameter follow explicit equations based on C and unit cell size. The equations empower the precise generation of gyroid structures with specified relative density, pore size, and strut diameter.

The mechanical properties and failure modes of gyroid structures strongly depend on the relative density. The quasi-static compression tests and simulations exhibited consistent results, indicating that increased relative density enhances the mechanical properties of the structures. Concurrently, Young's modulus and yield stress also exhibit positive power relationships with relative density. Stress and strain concentrations were observed at a 45° angle relative to the loading direction in gyroid structures with varying relative densities. The progressive failures and plateau regions in the stress–strain curves revealed the high deformability of porous gyroid structures. The bending-dominant behaviour and the fractures at a 45° angle during tests suggested shear load as the primary cause of failures.

Adjusting the loading direction influences the strut orientation and load transfer, thereby significantly affecting the mechanical response of gyroid structures. Under compressive load, different loading directions resulted in distinct mechanical properties and failure modes. Structures with struts more closely aligned with the loading direction demonstrated enhanced stiffness. These variations in mechanical properties, dictated by strut orientation, confirmed the anisotropic behaviour of gyroid structures.

In summary, this study contributed to understanding the geometric and mechanical properties of gyroid structures. The correlations and insights provide a robust foundation for the design and application of gyroid structures, particularly for biomedical implants. The ability to precisely tailor gyroid structures, guided by the correlations established in this study, offers the potential to create structures with enhanced functionality and performance.

Supplementary Materials: The following supporting information can be downloaded at: https://www.mdpi.com/article/10.3390/jmmp8060256/s1, Supplementary Data: Geometric correlations of gyroid structures.

Author Contributions: Conceptualization, C.H. and K.D.; methodology, C.H., B.V., and K.D.; formal analysis, C.H., M.G., and D.R.; investigation, C.H., M.G., and D.R.; resources, B.V. and K.D.; data curation, C.H., M.G., and D.R.; writing—original draft preparation, C.H., M.G., and D.R.; writing—review and editing, C.H., B.V., and K.D.; supervision, B.V. and K.D.; funding acquisition, B.V. and K.D. All authors have read and agreed to the published version of the manuscript.

Funding: This research was funded by the CELSA Research Fund and by Internal Funds KU Leuven.

Data Availability Statement: Data available on request due to privacy or ethical restrictions.

Conflicts of Interest: The authors declare no conflicts of interest.

References

1. Kapfer, S.C.; Hyde, S.T.; Mecke, K.; Arns, C.H.; Schröder-Turk, G.E. Minimal Surface Scaffold Designs for Tissue Engineering. *Biomaterials* **2011**, *32*, 6875–6882. [CrossRef] [PubMed]
2. Li, D.; Liao, W.; Dai, N.; Dong, G.; Tang, Y.; Xie, Y.M. Optimal Design and Modeling of Gyroid-Based Functionally Graded Cellular Structures for Additive Manufacturing. *Comput.-Aided Des.* **2018**, *104*, 87–99. [CrossRef]
3. Yuan, L.; Ding, S.; Wen, C. Additive Manufacturing Technology for Porous Metal Implant Applications and Triple Minimal Surface Structures: A Review. *Bioact. Mater.* **2019**, *4*, 56–70. [CrossRef] [PubMed]
4. Kosonen, T.; Kakko, K.; Raitanen, N. Evaluation of Pore Re-Opening after HIP in LPBF Ti–6Al–4V. *Powder Metall.* **2021**, *64*, 425–433. [CrossRef]
5. Liu, J.; Zhang, K.; Liu, J.; Zhang, R.; Zeng, Z.; Zhu, Y.; Huang, A. Discovering the Role of the Defect Morphology and Microstructure on the Deformation Behavior of Additive Manufactured Ti–6Al–4V. *Mater. Sci. Eng. A* **2022**, *859*, 144202. [CrossRef]
6. Cao, S.; Zou, Y.; Lim, C.V.S.; Wu, X. Review of Laser Powder Bed Fusion (LPBF) Fabricated Ti-6Al-4V: Process, Post-Process Treatment, Microstructure, and Property. *Light Adv. Manuf.* **2021**, *2*, 313–332. [CrossRef]
7. Savio, D.; Bagno, A. When the Total Hip Replacement Fails: A Review on the Stress-Shielding Effect. *Processes* **2022**, *10*, 612. [CrossRef]
8. Ataee, A.; Li, Y.; Fraser, D.; Song, G.; Wen, C. Anisotropic Ti-6Al-4V Gyroid Scaffolds Manufactured by Electron Beam Melting (EBM) for Bone Implant Applications. *Mater. Des.* **2018**, *137*, 345–354. [CrossRef]
9. Musthafa, H.-S.N.; Walker, J.; Rahman, T.; Bjørkum, A.; Mustafa, K.; Velauthapillai, D. In-Silico Prediction of Mechanical Behaviour of Uniform Gyroid Scaffolds Affected by Its Design Parameters for Bone Tissue Engineering Applications. *Computation* **2023**, *11*, 181. [CrossRef]
10. Yang, L.; Wu, S.; Yan, C.; Chen, P.; Zhang, L.; Han, C.; Cai, C.; Wen, S.; Zhou, Y.; Shi, Y. Fatigue Properties of Ti-6Al-4V Gyroid Graded Lattice Structures Fabricated by Laser Powder Bed Fusion with Lateral Loading. *Addit. Manuf.* **2021**, *46*, 102214. [CrossRef]
11. Liu, Y.; Rath, B.; Tingart, M.; Eschweiler, J. Role of Implants Surface Modification in Osseointegration: A Systematic Review. *J. Biomed. Mater. Res. A* **2020**, *108*, 470–484. [CrossRef] [PubMed]
12. Hameed, P.; Liu, C.-F.; Ummethala, R.; Singh, N.; Huang, H.-H.; Manivasagam, G.; Prashanth, K.G. Biomorphic Porous Ti6Al4V Gyroid Scaffolds for Bone Implant Applications Fabricated by Selective Laser Melting. *Prog. Addit. Manuf.* **2021**, *6*, 455–469. [CrossRef]
13. Walker, J.M.; Bodamer, E.; Kleinfehn, A.; Luo, Y.; Becker, M.; Dean, D. Design and Mechanical Characterization of Solid and Highly Porous 3D Printed Poly(Propylene Fumarate) Scaffolds. *Prog. Addit. Manuf.* **2017**, *2*, 99–108. [CrossRef]
14. Schoen, A.H. *Infinite Periodic Minimal Surfaces Without Self-Intersections*; NASA Electronics Research Center: Cambridge, MA, USA, 1970.
15. R Core Team. *R: A Language and Environment for Statistical Computing*; R Core Team: Vienna, Austria, 2021.
16. Vrancken, B.; Thijs, L.; Kruth, J.-P.; Van Humbeeck, J. Heat Treatment of Ti6Al4V Produced by Selective Laser Melting: Microstructure and Mechanical Properties. *J. Alloys Compd.* **2012**, *541*, 177–185. [CrossRef]
17. Ashby, M.; Evans, A.; Fleck, N.; Gibson, L.; Hutchinson, J.; Wadley, H.; Delale, F. Metal Foams: A Design Guide. *Appl. Mech. Rev.* **2001**, *54*, B105–B106. [CrossRef]
18. Gibson, L.J. Mechanical Behavior of Metallic Foams. *Annu. Rev. Mater. Sci.* **2000**, *30*, 191–227. [CrossRef]
19. Yang, L.; Yan, C.; Fan, H.; Li, Z.; Cai, C.; Chen, P.; Shi, Y.; Yang, S. Investigation on the Orientation Dependence of Elastic Response in Gyroid Cellular Structures. *J. Mech. Behav. Biomed. Mater.* **2019**, *90*, 73–85. [CrossRef]
20. Yan, C.; Hao, L.; Yang, L.; Hussein, A.Y.; Young, P.G.; Li, Z.; Li, Y. Chapter 6—Numerical Analysis on the Mechanical Properties of Uniform TPMS. In *Triply Periodic Minimal Surface Lattices Additively Manufactured by Selective Laser Melting*; Yan, C., Hao, L., Yang, L., Hussein, A.Y., Young, P.G., Li, Z., Li, Y., Eds.; 3D Printing Technology Series; Academic Press: Cambridge, MA, USA, 2021; pp. 183–217. ISBN 978-0-12-824438-8.
21. Song, C.; Chen, J.; Lei, H.; Yang, Z.; Deng, Z.; Li, Y.; Wang, J.; Yang, Y.; Han, C. Radial Gradient Design Enabling Additively Manufactured Low-Modulus Gyroid Tantalum Structures. *Int. J. Mech. Sci.* **2024**, *262*, 108710. [CrossRef]
22. Torres-Sanchez, C.; Al Mushref, F.R.A.; Norrito, M.; Yendall, K.; Liu, Y.; Conway, P.P. The Effect of Pore Size and Porosity on Mechanical Properties and Biological Response of Porous Titanium Scaffolds. *Mater. Sci. Eng. C* **2017**, *77*, 219–228. [CrossRef]
23. Parisien, A.; ElSayed, M.S.A.; Frei, H. Mechanoregulation Modelling of Stretching versus Bending Dominated Periodic Cellular Solids. *Mater. Today Commun.* **2022**, *33*, 104315. [CrossRef]
24. Parisien, A.; ElSayed, M.S.A.; Frei, H. Mature Bone Mechanoregulation Modelling for the Characterization of the Osseointegration Performance of Periodic Cellular Solids. *Materialia* **2022**, *25*, 101552. [CrossRef]
25. Li, L.; Shi, J.; Zhang, K.; Yang, L.; Yu, F.; Zhu, L.; Liang, H.; Wang, X.; Jiang, Q. Early Osteointegration Evaluation of Porous Ti6Al4V Scaffolds Designed Based on Triply Periodic Minimal Surface Models. *J. Orthop. Transl.* **2019**, *19*, 94–105. [CrossRef] [PubMed]

26. Yao, Y.; Qin, W.; Xing, B.; Sha, N.; Jiao, T.; Zhao, Z. High Performance Hydroxyapatite Ceramics and a Triply Periodic Minimum Surface Structure Fabricated by Digital Light Processing 3D Printing. *J. Adv. Ceram.* **2021**, *10*, 39–48. [CrossRef]
27. Barba, D.; Alabort, E.; Reed, R.C. Synthetic Bone: Design by Additive Manufacturing. *Acta Biomater.* **2019**, *97*, 637–656. [CrossRef]
28. Yang, L.; Yan, C.; Cao, W.; Liu, Z.; Song, B.; Wen, S.; Zhang, C.; Shi, Y.; Yang, S. Compression–Compression Fatigue Behaviour of Gyroid-Type Triply Periodic Minimal Surface Porous Structures Fabricated by Selective Laser Melting. *Acta Mater.* **2019**, *181*, 49–66. [CrossRef]
29. Fan, Z.; Huang, G.; Lu, Y.; Chen, Y.; Zeng, F.; Lin, J. Full Compression Response of FG-Based Scaffolds with Varying Porosity via an Effective Numerical Scheme. *Int. J. Mech. Sci.* **2022**, *223*, 107294. [CrossRef]
30. Cutolo, A.; Engelen, B.; Desmet, W.; Van Hooreweder, B. Mechanical Properties of Diamond Lattice Ti–6Al–4V Structures Produced by Laser Powder Bed Fusion: On the Effect of the Load Direction. *J. Mech. Behav. Biomed. Mater.* **2020**, *104*, 103656. [CrossRef]
31. Morgan, E.F.; Unnikrisnan, G.U.; Hussein, A.I. Bone Mechanical Properties in Healthy and Diseased States. *Annu. Rev. Biomed. Eng.* **2018**, *20*, 119–143. [CrossRef]
32. Liu, B.; Wang, H.; Zhang, N.; Zhang, M.; Cheng, C.-K. Femoral Stems With Porous Lattice Structures: A Review. *Front. Bioeng. Biotechnol.* **2021**, *9*, 772539. [CrossRef]
33. Han, C.; Wang, Y.; Wang, Z.; Dong, Z.; Li, K.; Song, C.; Cai, C.; Yan, X.; Yang, Y.; Wang, D. Enhancing Mechanical Properties of Additively Manufactured Voronoi-Based Architected Metamaterials via a Lattice-Inspired Design Strategy. *Int. J. Mach. Tools Manuf.* **2024**, *202*, 104199. [CrossRef]
34. Challis, V.J.; Xu, X.; Zhang, L.C.; Roberts, A.P.; Grotowski, J.F.; Sercombe, T.B. High Specific Strength and Stiffness Structures Produced Using Selective Laser Melting. *Mater. Des.* **2014**, *63*, 783–788. [CrossRef]
35. Cuadrado, A.; Yánez, A.; Martel, O.; Deviaene, S.; Monopoli, D. Influence of Load Orientation and of Types of Loads on the Mechanical Properties of Porous Ti6Al4V Biomaterials. *Mater. Des.* **2017**, *135*, 309–318. [CrossRef]
36. Wu, Z.; Narra, S.P.; Rollett, A. Exploring the Fabrication Limits of Thin-Wall Structures in a Laser Powder Bed Fusion Process. *Int. J. Adv. Manuf. Technol.* **2020**, *110*, 191–207. [CrossRef]
37. Kranz, J.; Herzog, D.; Emmelmann, C. Design Guidelines for Laser Additive Manufacturing of Lightweight Structures in TiAl6V4. *J. Laser Appl.* **2014**, *27*, S14001. [CrossRef]
38. Shange, M.; Yadroitsava, I.; du Plessis, A.; Yadroitsev, I. Roughness and Near-Surface Porosity of Unsupported Overhangs Produced by High-Speed Laser Powder Bed Fusion. *3D Print. Addit. Manuf.* **2022**, *9*, 288–300. [CrossRef]
39. Hou, C.; Sinico, M.; Vrancken, B.; Denis, K. Investigation of the Laser Powder Bed Fusion Manufacturing Process and Quasi-Static Behaviour of Ti6Al4V Voronoi Structures. *J. Mater. Process. Technol.* **2024**, *328*, 118410. [CrossRef]